Multi-scale Digital Rock: Application of a multi-scale multi-phase workflow to a Carbonate reservoir rock

Andrew Fager[1], *Hiroshi* Otomo[1], *Rafael* Salazar-Tio[1], *Ganapathi* Balasubramanian[1], *Bernd* Crouse[1], *Raoyang* Zhang[1], *Hudong* Chen[1], *and Josephina* Schembre-McCabe[2]

[1]Dassault Systèmes, USA
[2]Chevron, USA

Abstract. In some of the challenging digital rock applications the trade-off between model resolution and representative elemental volume is not captured in a single resolution model satisfying the minimum requirements for both aspects. In the wide range of lithofacies found in carbonate reservoir rocks, some facies fall in this category, where large pores, ooids or vugs, are connected by small scale porous structures that could have orders of magnitude smaller pores. In these cases a multi-scale digital rock approach is needed. We recently developed an extension to a digital rock workflow that includes a way to handle sub-resolution pore structures in single phase and multi-phase flow scenarios in addition to regular resolvable pore structures. Here we present an application of this methodology to a multi-scale limestone carbonate rock. A microCT image captures the large pores for this sample, but does not resolve all the pores smaller than the pixel size. A three phase image segmentation that considers pore, solid and under-resolved pores or porous media (PM) is generated. A high resolution confocal image model is obtained for a representative region of the smaller pores or PM region. A set of constitutive relationships (namely permeability vs. porosity, capillary pressure vs saturation and relative permeability vs saturation) are obtained by simulation from the high resolution confocal model. The low resolution segmented image, a porosity distribution image, and the constitutive relationships for the PM are input in an extended LBM multi-scale multi-phase solver. First we present results for absolute permeability and show a parametric study on PM permeability. The model recovers the expected behaviour when the PM regions are considered pore or solid. A consistent value of permeability with experiments is obtained when we use the PM permeability from the high resolution model. To demonstrate the multi-phase behaviour, we present results for capillary pressure imbibition multi-scale simulations. Here a small model for a dual porosity system is created in order to compare single scale results with the multi-scale solver. Finally, capillary imbibition results for the whole domain are shown and different wettability scenario results are discussed. This application illustrates a novel multi-scale simulation approach that can address a long standing problem in digital rock.

1 Introduction

Petrophysical properties are critical to understand and forecast oil & gas production. In particular, properties related to single-phase and multi-phase fluid flow are required. These properties represent effective macroscopic constitutive relationships for flow; such as absolute permeability vs porosity, J-function capillary pressure and relative permeability vs. saturation. Laboratory measurements are typically done for this purpose, but another option is to use digital rock to simulate petrophysical properties directly using the particular rock 3D structure, obtained using x-ray micro-tomography (microCT) [1]. Properties directly depend on the internal pore structure, and different type of structures have different constitutive relationships; for example; random porous media, packed spheres, parallel planes, bundle of tubes, heterogeneous sandstones, shale rocks, carbonate rocks. No single property model is good for all porous media types, therefore the need of laboratory measurements or simulation on the actual 3D image of the particular rock. Samples that belong to one porous media type will share similar constitutive relationships. This is the reasoning behind core sampling per porous media type.

A typical microCT image resolution can be few micro-meter per pixel. For most sandstones this resolution may capture the main percolation pore space, while small crevices and some clay porosity are not captured. Since the main percolating path is primarily responsible for fluid flow, this image could still represent the flow properties of the rock. But in many other cases the pores (bodies and throats) that form the interconnected pore structure can vary in size in the same rock by orders of magnitude. This case can be found in some carbonate rock lithofacies, which are complex structures form by recrystallization of micro-organisms, where larger pores are many times connected only through pores smaller than the typical microCT image resolution, which is not able to capture the main percolating pore structure and is not suitable for flow simulation. An increase in imaging resolution can enable percolation, but with more magnification, the larger pores are not going to be captured properly by the image. This is a genuine example where a multi-scale approach is needed to enable simulation.

* Corresponding author: Andrew.FAGER@3ds.com

In the digital rock literature, there are several publications on multi-scale extensions of multi-phase pore-network models [26-27]. Regarding voxel based models, like LBM, there are several publications [2-6, 24-25] on single-phase multi-scale fluid flow simulations, where formulations for a viscous force with the permeability has been provided by the Brinkman equation and the permeability value was derived from simulations at finer resolutions, but extensions to the multi-phase flow simulation are not discussed. Two recent publications [7, 8] consider multi-phase fluid flow in multi-scale pore structures. In [7] relative permeability from under-resolved regions was computed by solving the transport equation for the total energy, Helmholtz free and kinetic energy, but without considering other important physical properties such as the capillary-pressure curves. On the other hand, in [8], the capillary saturations are calculated in the finer scale using a Young-Laplace relationship and used for estimating capillary pressure in under-resolved regions, but no fluid flow simulation was performed involving pore structure connectivity and relative permeability was also not considered.

We present in this paper an application of a recently developed [9-10] extension to the Shan-Chen multi-phase Lattice Boltzmann model [11-15] that introduces numerical models for treating multi-scale porous media, such as carbonate rocks, which includes under-resolved pores as well as resolved pores. The flow behaviour of under-resolved pores (porous media) is described by a complete set of multi-phase constitutive relationships, which includes single phase permeability-porosity correlation, relative-permeability-saturation, and capillary-pressure-saturation curves. This approach allows for local variability of porosity and saturation in under-resolved regions, while fluid forces are applied locally satisfying the constitutive relationships in the porous media. In the rest of this section we describe our general workflow for multi-scale simulations, as well as describe the carbonate sample selected for this application. In the next section we demonstrate the workflow steps, including image segmentation, porosity estimation, and porous media characterization, all required inputs for the multi-scale multi-phase simulation. Finally we discuss the results for single-phase and multi-phase and present our conclusions.

1.1 Multi-scale modelling

Current microCT technologies focus on imaging one single scale, and requires one to choose this scale by balancing the trade-off between image resolution and representative elemental volume (REV). Image resolution must be at least small enough to resolve a percolating pore structure, while REV must be at least large enough to statistically represent all sizes of pores found in the sample. Unfortunately, the number of pixels in microCT imaging systems is limited, and constrains the pixel size and REV to each other. In cases where pore sizes vary by orders of magnitude, like carbonate rocks, a compromise between pixel size and REV cannot be found, and porous media (PM) pixels have to be considered. PM pixels represent regions where pores are present but smaller than the pixel size. An example of a Carbonate rock [21] image is shown in figure 1 (top), where some regions showing as intermediate grey can be identified as PM, with pores sizes smaller than the pixel size. The intermediate grey value can be interpreted as the pore fraction or sub-resolution porosity, between 100% pore (darkest regions) and 0% pore (brightest regions). In general the sub-resolution porosity of PM pixels can be different, even if the pixels belong to the same PM-type. In a similar way that core samples can be classified by porous media types, PM pixels can also be classified by PM-types if they share similar constitutive relationships, or equivalently similar 3D pore structure, as illustrated in figure 1. High resolution imaging, like scanning electron microscopy (SEM) can be used to identify and select representative sample images for a PM-type, for instance in a carbonate rock like the one in figure 1, we could find that all the under-resolved pixels belong to a single PM-type, that we could call “carbonate PM-type 1” for instance.

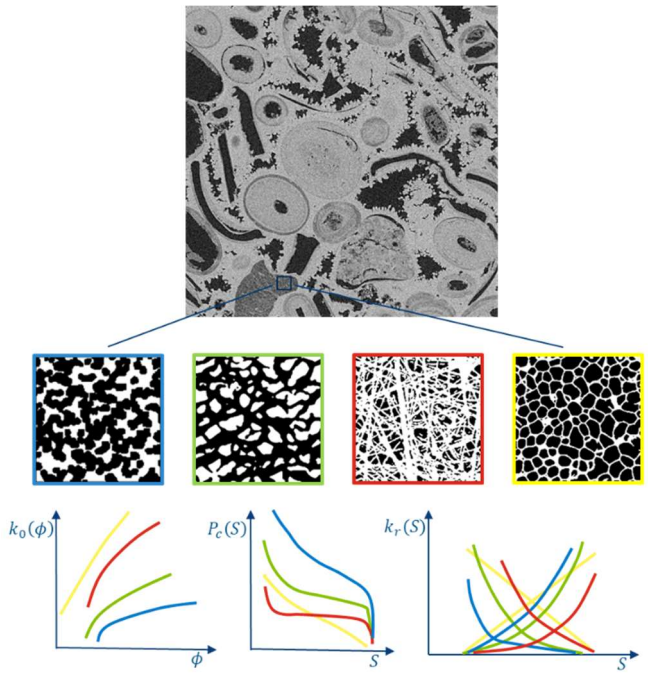

Fig. 1. Modelling of under-resolved pore structures using the concept of PM-types classification and characterization.

In general, it could be possible to have more than one PM-type present in an image, corresponding to different sub-resolution pore structures. A rock can have few clay minerals, with distinct microscopic pore structure, like kaolinite that exhibits typical booklet or book-like structures, grown diagenetically inside pores, Illite is hairy grain coating, and chlorite forms flakes. Microporous carbonates can be also present in rocks, as well as partially dissolved feldspars and other metamorphic microporous rocks. In shale rocks organic content, like kerogen also have a microporous structure. Each of these PM-types will behave differently under fluid flow and their identification is part of the image segmentation process. In many cases, like the carbonate rock example in figure 1, a single PM-type can be sufficient.

In order to sample 3D structures of a given PM-type, a combination of high resolution imaging techniques can be

used, for example: SEM, focus ion-beam (FIB), laser confocal scanning microscopy (LCSM), X-ray nano-tomography are the most common. By performing simulations using 3D images of these PM samples, it is possible to obtain a suitable set of constitutive relationships that represents well the corresponding PM-type as illustrated in figure 1 (bottom). In a sense, the constitutive relationships for these PM-types can be seen in turn as the result of high resolution digital rock simulations of micron size models. These relationships, absolute permeability vs porosity, J-function capillary pressure and relative permeability vs. saturation, describe a continuum behaviour where porosity, saturation and other properties are described as continuum variables in contrast to a discrete representation where each pixel is pore or solid. It is feasible that some representative PM-types can be characterized and collected into PM libraries that could be used in the same way as core samples called "analogues" are used in core analysis, in this case as a convenient complement to high resolution imaging.

These PM pixels with their local porosity estimated from the images and corresponding constitutive relationships should be sufficient input for a continuous solver that simulates the interaction between such PM pixels. Moreover, the challenge is on extending the current digital rock solvers from only pore/solid pixels to include also PM pixels in the algorithms. Here, we use a solution based on the lattice Boltzmann method (LBM), although the methodology itself is not limited to LBM, for this issue by employing a new workflow [9-10] with effective computational models for flows in under-resolved porous regions. In a fluid-flow simulation at a certain resolution level, flow contributions from under-resolved porous regions are properly taken into account by applying numerical models at each location using local information of geometry and fluids. The models reproduce proper forces acting on the fluids such as viscous, pressure, and capillary forces, using local representative physical properties captured by the PM-type constitutive relationships.

There are various ways to define numerical models for fluid forces in the under-resolved region. We show here one possible example [9-10]. The viscous force $\vec{F}^{\alpha}_{PM\_vis}$ can be defined using the absolute permeability K_0 and relative permeability K_r^{α} as,

$$\vec{F}^{\alpha}_{PM\_vis} = -\frac{\nu^{\alpha}}{K_0 K_r^{\alpha}} \rho^{\alpha} \vec{u}^{\alpha} \qquad (1)$$

where α is an index for fluid phases and ν is the kinematic viscosity. Here, ρ and $\vec{u}$ are density and velocity of fluid flow, respectively. Also, K_0 and K_r^{α} are functions of the porosity ϕ and density ratio of fluid phases under an assumption of homogeneous structure for under-resolved porous region. On the other hand, an example for definition of capillary force $\vec{F}^{\alpha}_{PM\_cap}$ can be written as,

$$\vec{F}^{\alpha}_{PM\_cap} = -\frac{2\sigma cos\theta J}{\sqrt{K_0 K_r^{\alpha}/\phi}} \left(\widehat{\nabla \rho^{\alpha_1}}\right) \cdot H(At, |\partial_x(At)|) \qquad (2)$$

where the hat notation indicates the unit vector and θ is the fluid-solid contact angle in the under-resolved porous structure. Here, J is the Leverett J-function, $P_c\sqrt{K_0 K_r^{\alpha}/\phi}/\sigma cos\theta$, is the normalized capillary function of density ratio of fluid phases, and α_1 is an index of a corresponding fluid phase. A function H is a switch function depending on the local multi-phase interface information. Here, $At = (\rho^{\alpha_1} - \rho^{\alpha_2})/(\rho^{\alpha_1} + \rho^{\alpha_2})$. This switch function is necessary for the diffusive multi-phase model because its non-zero interface thickness may cause excessive artificial force. Moreover, this definition cannot cover a scenario where a fluid phase is confined in an under-resolved pixel. In order to mitigate this problem, an additional model can be implemented using the Leverett J-function and local pressure. Since the saturation is almost insensitive to the local pressure force in this scenario, the local expected saturation level can be computed accurately using the local pressure and the Leverett J-function. Accordingly, the local saturation is controlled without significant deviation from the expected value.
Accurate wettability can be realized with the Shan-Chen model in the LBM approach, which naturally constructs the inter-component force using the fluid potential from neighboring sites [9-13]. On the solid boundary, the proper wall potential is assigned so that the targeted contact angle is achieved. By simply extending this model, the wettability originated from solid parts in the porous media can be properly taken into account. Specifically, the potential in the porous media is constructed by both fluid density and solid wall potential weighted by local porosity.

1.2 Test sample

For this study, we use an Indiana limestone rock sample with porosity and permeability measurements in a 1.5 inch diameter core-plug sample, summarized in table 1. Mercury Intrusion Porosimetry (MIP) characterization was done in a 0.25 inch end-trim for this sample and results are shown in figure 2, including the saturation vs. pressure measured data and the derived pore throat size distribution, where two pore size families are clearly appreciated. To study the oil-water behaviour in this Indiana limestone core-plug sample, a spontaneous counter-current imbibition experiment in a decane-saturated and decane-aged sample was done, yielding a remaining decane saturation of 38%.

Table 1. Porosity, permeability laboratory measurements.

	un-stressed	**800 psi**
Klinkenberg Permeability, mD	12.5	6.68
Permeability to Air, mD	14.6	7.94
Swanson Permeability, mD	10.3	-
He Porosity, fraction	0.17	0.16

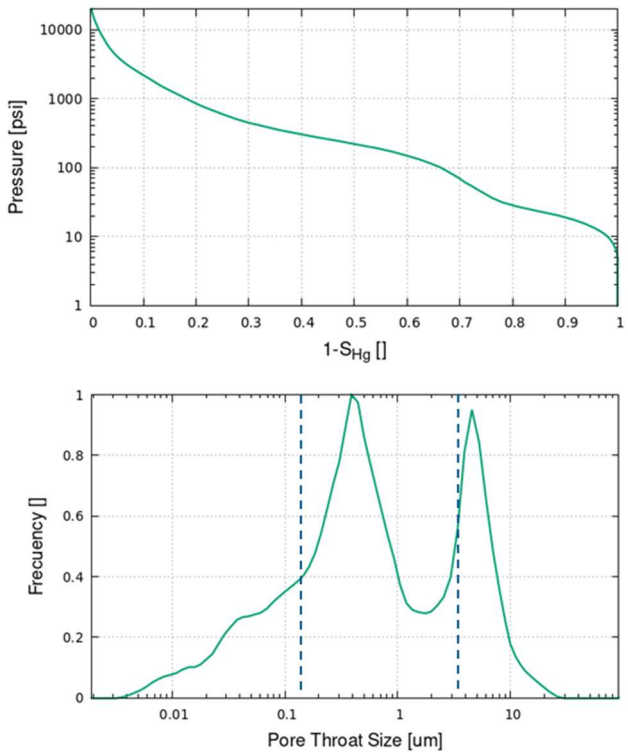

Fig. 2. Mercury intrusion porosimetry data, and derived pore throat size distribution of Indiana limestone sample

Imaging was acquired at two resolutions, 3.5 μm/pixel x-ray micro-tomography 3D imaging, shown in figure 3 for a selected 600^3 volume, and laser confocal scanning microscopy at 0.128 μm/pixel, shown in figure 4. A statistical reconstruction algorithm [22] used a set of 2D confocal images focused at a typical micro-porous region as input to build a representative 3D model. The multi-point statistical (MPS) reconstruction method [22] was developed, validated and used extensively for geomodeling applications, and is well known by his capability to capture high order correlations beyond 2-point correlation functions or variograms. Although, we have not done and extensive validation for pore-scale modeling applications, the MPS reconstruction is not a required element in our workflow, which can use in general any other type of higher resolution 3D imaging, like nanoCT and FIB.

We show with vertical dashed lines in figure 2, these two imaging resolutions as a reference of what pore sizes can be captured and modelled using each of these imaging techniques.

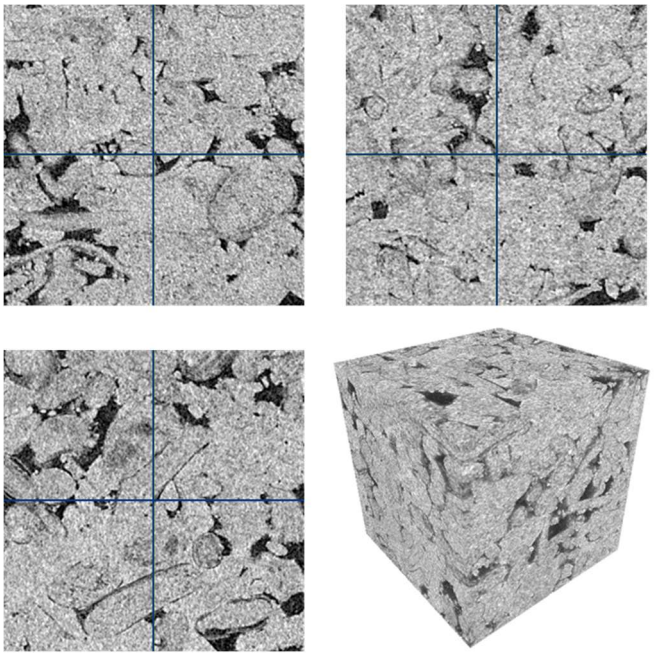

Fig. 3. Cross-sectional view and 3D view of the microCT image for our application sample, Indiana Limestone.

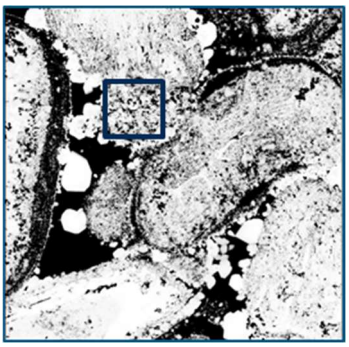

Fig. 4 View of a slide of confocal image in the Indiana Limestone sample, at nominal resolution of 0.128 μm/pixel.

2 Multi-scale workflow

In this section we follow the multi-scale workflow steps for the carbonate sample described in the previous section. A summary of the workflow steps is shown in figure 5, which includes: large scale modelling: segmentation, porosity estimation, small scale modelling: PM samples selection, properties simulation using digital rock, and generation of constitutive relationships for the PM-type. We perform our multi-scale flow simulations using these inputs from both scales, and the results are presented and discussed in the following section.

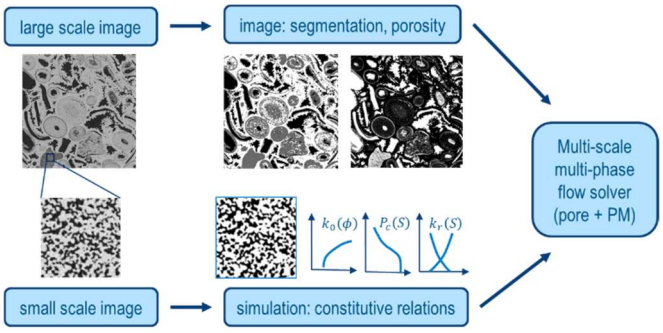

Fig. 5. Multi-scale workflow.

2.1 Image segmentation, porosity

MicroCT images show a grey scale that quantify the x-ray attenuation coefficient of the material contained in each pixel. Different pure materials (minerals and fluids) have different attenuations values and show as different grey scale values. If each pixel contains only one type of material, segmentation reduces to locate the best thresholds that separate grey scale values corresponding to different materials. However, when a pixel contains pores smaller than the pixel size, a.k.a PM pixel, there is a partial volume effect and the x-ray attenuation is an average of the solid and pore fractions within the PM pixel.

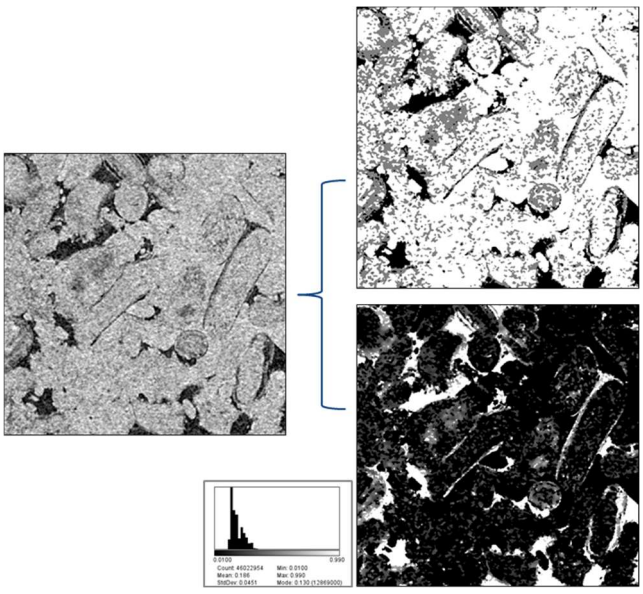

Fig. 6. Generation of image segmentation and image porosity.

Depending on the how different the PM pixel grey values are compared to other materials present on the image, it may be possible to use only thresholding to segment the PM pixels from the other pure materials. If grey scale is not enough, textural features can also be used to segment out PM pixels of different PM-types. In the Indiana Limestone sample presented in the previous section, we identify one PM-type, corresponding to a crystalline micro-structure sometimes referred as micrite. We show in figure 6 (top-right) a possible segmentation for our Indiana Limestone image, where pixels of pore/solid show as black/white, while pixels for the PM-type "micrite" are marked with a single shade of medium grey. The volume fraction of pore pixels in the image is 7%, while the volume fraction of PM pixels is 21.3%.

Next, we estimate the values for the local porosity in each of the pixels marked as PM. We use the segmented image to mask out each of the three sub-sets of pixels in the original grey scale image in figure 6 (left). We compute the average grey scale value for the two sub-sets corresponding to pore and solid pixel labels. These two grey scale values should correspond to the values of porosity 1.0 and 0.0 respectively. A linear transform between grey scale values and porosity is calibrated using these two reference points. Notice that this transformation is only possible in cases with only one type of mineral. In general, a linear transform can also be applied using an estimation for the mean value and standard deviation of the porosity in the PM region. In addition to the calibration of grey scale to porosity, a masked Gaussian smoothing filter can be applied to reduce the noise level for the PM porosity. The result for the local porosity image is shown in figure 6 (bottom-right), with a PM porosity mean and standard deviation of 0.186 and 0.05 respectively and a histogram distribution shown next to the porosity image. Notice that the porosity values in the pixels labelled as pore and solid are 1.0 and 0.0 respectively, this is enforced by the masking criteria. A quick calculation of the total porosity for this sample image, including the two contributions from pore and PM is: 7% + 0.186*21.3% = 11%. A more accurate way to map the under-resolved porosity is by direct measurement, using an x-ray attenuating contrast agent like Iodine in a brine solution that is vacuum saturated in the sample. A reference dry-microCT (unsaturated) is performed first, and used later to subtract from the wet-microCT (saturated). This differential imaging technique has demonstrated quantitative accuracy for estimating the under-resolved porosity [30-32] and robustness regarding different mineralogy, therefore it is not limited by lithology. However, the availability of this imaging technique seem to be mainly in research laboratories, being a less common capability in commercial microCT facilities. If only dry microCT is available, the method described earlier can still be used.

These two images: (1) PM-type label and (2) sub-resolution porosity, can be sufficient input for a complete description of flow behaviour of the PM pixels; assuming that a PM library of constitutive relationship curves is accessible for the LBM solver to fetch the corresponding flow response of each PM pixel given its pair values of: PM-type and sub-resolution porosity. In the next sub-section we present the required PM library of constitutive relationship.

2.2 Porous media models

Based on [28-29], "micrite" particles are classified in three classes; fine, medium and coarse micrites, with a diameter (or maximum side length of the crystal) of 0.1-3μm, 3-6μm and 6-10 μm, respectively. They exhibit a relation between micropore classes and micrite microtextures: Very fine micropores (0.1 – 2 μm) are found in compact anhedral micrites (like shown in figure 7), coarse micropores (6 – 10 μm) are found in microrhombic and polyhedral micrites. Care

should be taken to choose the correct PM-type representative sample if direct imaging is not available. In this application, for modelling the identified micrite PM-type, a model was obtained by LCSM microscopy imaging in a selected representative location of the identified micrite PM-type in the Indiana Limestone sample. A 3D model was constructed from those confocal images with a resolution of 200 nanometres. An image of the confocal model is shown in figure 7.

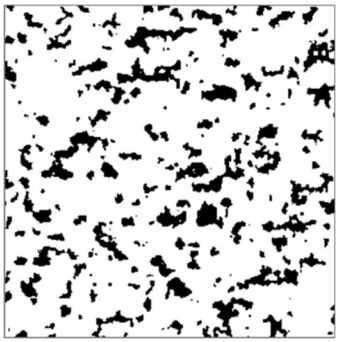

Fig. 7. PM model for the micrite PM-type, based on confocal imaging

The porosity, permeability values for the confocal model are 18.2%, 1.7mD. We use the confocal model for micrite as it comes from a high resolution image of the actual sample. Fluid flow simulations using our single-scale LBM solver produce a set of constitutive relationships, as illustrated in figure 8, absolute permeability vs porosity, capillary pressure vs. saturation and relative permeability vs. saturation, for the micrite PM-type represented by the confocal PM model, shown in figure 7.

In order to capture the single phase absolute permeability correlation with porosity we consider the simulation results from eight sub-volumes and fit a parametric relationship as show in figure 8 (top). The fitting quality can be affected by the functional form used, and the limited data range, however the application range is also limited, 12%-24% from the porosity distribution in figure 6, with the maximum of the distribution where the actual data is found. For two-phase flow simulations, we consider in this case an imbibition setup (inlet water, outlet oil) and fit similar parametric relationships in order to capture continuous functions of saturation conveniently, figure 8 (Pc middle, Kr bottom). The wettability condition was set to water wet, with a water-contacted angle of 10°, oil-contacted angle 30°, a water-oil interfacial tension of 30 dynes/cm, and an initial water saturation of approximately 35%. The set of curves in figure 8 will be use as the constitutive relationships that represent the flow behaviour of the PM pixels classified as belonging to the PM-type identified as micrite for our Indiana Limestone sample in the multi-scale simulations presented in the next section.

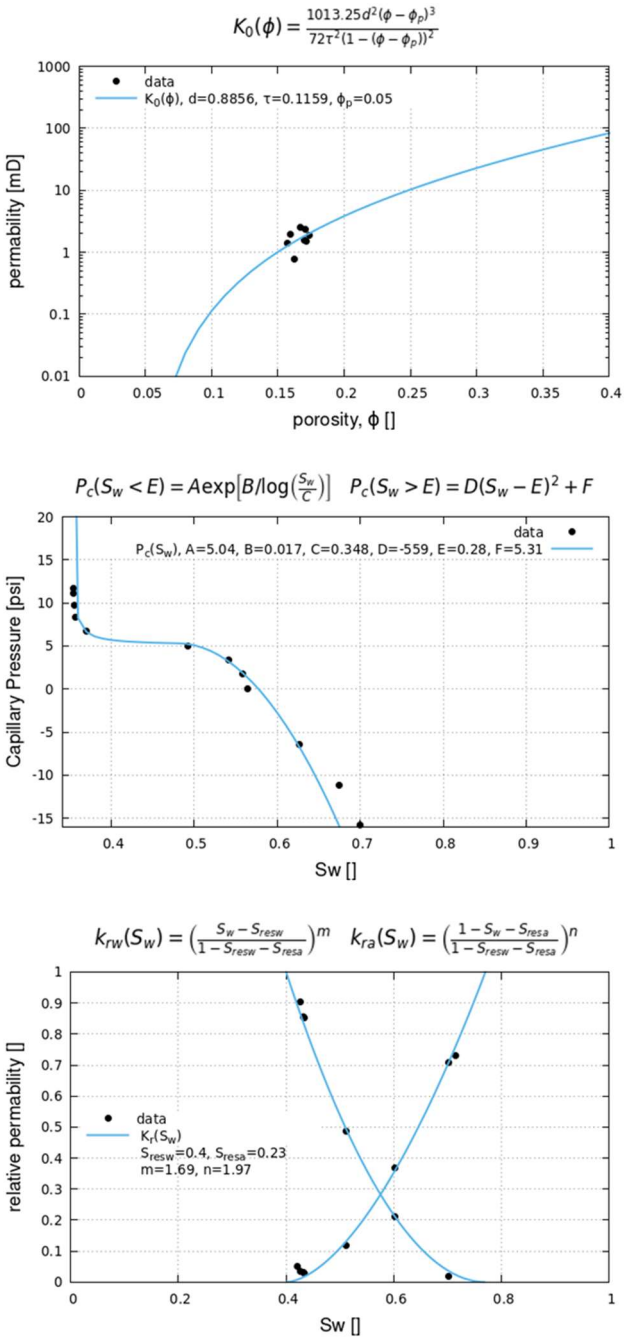

Fig. 8. Constitutive relationships for the confocal model of micrite PM-type.

3 Results and discussion

As a baseline for comparison we would like to consider two references: (1) A single resolution model, where in figure 6 (top-right) all the pixels marked as PM are re-labelled as solid, and (2) a registered model, which is a full resolution dual porosity model, constructed by scaling the microCT model by a factor of 10×, and replace the PM regions by copies of the 3D PM model, shown in figure 7, using periodic mirror boundaries that enforce full connectivity of the PM pore structure.

In figure 9 we show an illustration of this registered model constructed using the confocal model pore structure. The top image shows a slice from the resulting 6000^3 pixels

model, with a resolution of 0.35 μm/pixel, which is 10 times smaller than the original microCT image resolution. The full model shown in figure 9 is too large to be used in a simulation, therefore we will use sub-volumes or coarsened versions of this model for comparison.

In this section we discuss the single-phase and multi-phase multi-scale simulation results for our Indiana Limestone sample and compare them with the available experimental measurements and our baseline simulation results.

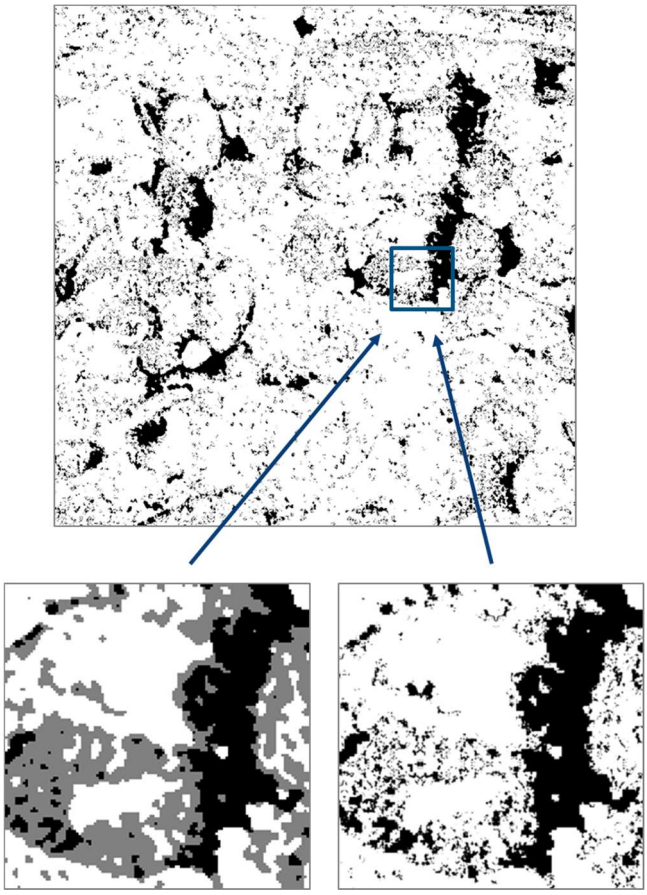

Fig. 9. Registered confocal model, 6000^3.

3.1 Single phase

As shown in the pore size distribution from figure 2 (bottom), the microCT resolution of 3.5 μm can only fully resolve the larger pores of this Indiana Limestone sample, not the micro-pores. Moreover, when we analyse the connectivity of the fully resolved percolating pore structure, we find that the critical pore throat is just 1 pixel. This means that the single-scale pore structure (PM considered solid), is barely connected. In order to obtain a numerically stable estimation of the baseline permeability for the single resolution model, we increase the resolution in the model by a factor of 2×. The single-scale single-phase LBM solver simulation result for absolute permeability using the 2× model is 7.7 mD (the 1× model result is 6.0 mD). We select a representative direction (k_x) in order to facilitate the comparison between different results. The velocity flow paths for this single resolution model are show in figure 10 (left). Next, we consider the registered large size model described in the introduction of this section. We utilize a surface element based LBM modelling capability [16-20] to capture features below the nominal pixel resolution by using as input geometry a grey scale image of the pore-solid boundary. This grey scale boundary interface is actively used to locate a pore-solid surface out of the original pixel restricted grid, allowing us effectively to resolve pore structures smaller than the nominal pixel size, and avoid "stair case" related artefacts in the flow. We nominally coarsen our 6000^3 registered by a 5× factor, however the grey scale resulting model could be considered equivalent to a 2400^3 model. The registered confocal model simulation result for absolute permeability is 8.2 mD. Velocity flow paths for this registered model are shown in figure 10 (right). This small increment in the registered model result relative to the single resolution model permeability indicates that the role of the under-resolved porosity for single-phase flow is secondary in the case of this sample.

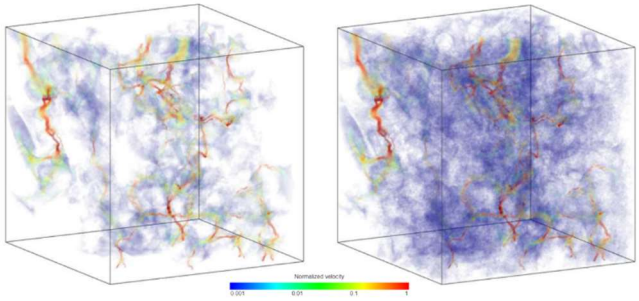

Fig. 10. Velocity flow lines for single resolution model (left) and registered confocal model (right).

For the multi-scale single-phase simulation in this Indiana Limestone sample, following the workflow in figure 5, we use as geometry input the pair of images for the segmentation and porosity, figure 6 (right), and the porosity vs permeability relationship for the confocal model of micrite PM-type shown in figure 8 (top). The multi-scale simulation result for absolute permeability is 7.8 mD, which is a value consistent with the results from the single resolution model and registered model simulations.

Finally we want to discuss a parametric study for the overall single-phase flow in this sample as a function of a varying value of the PM permeability. The goal of this exercise is to verify the consistency between our single-scale solver and our multi-scale solver: for a small enough value of k_{PM} used in our multi-scale solver we should recover the same results as in our single-scale solver when PM pixels are re-labelled as solid. Similarly, for a large enough value of k_{PM} used in our multi-scale solver, we should recover the same results as in our single-scale solver when PM pixels are re-labelled as pore. The results of this parametric study are shown in figure 11. As expected we recover with our multi-scale solver the respective end member results of the single-scale solver for the overall permeability. Moreover, we show in figure 11 that the range of the permeability expected from laboratory measurements, table 1, is consistent with the result obtained with the confocal model we use for micrite PM-type.

This kind of response function in figure 11, can also be useful to understand the ranges of permeability for the under-resolved porosity where a significant impact in the overall flow can be expected. This response function is not trivial and depends on the complexity of the PM plus pore connected structure.

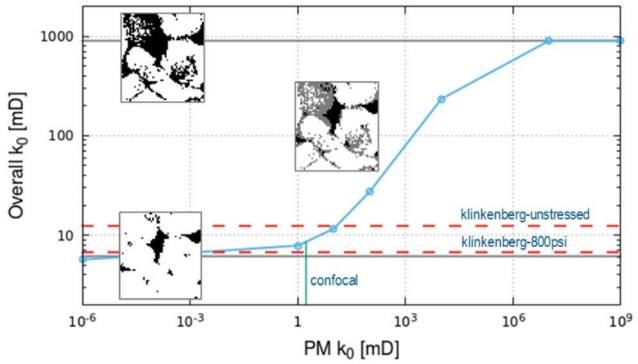

Fig. 11. Single-phase multi-scale flow permeability prediction as function of PM permeability

3.2 Multi-phase drainage

Although it is entirely possible to use it for drainage, we will delay the use of our multi-scale multi-phase LBM extension until the next sub-section for imbibition, which represent a more interesting scenario for oil-water behaviour, and has some experimental data to compare with, while in the other hand for drainage we have only MIP experimental data to compare with, therefore we take this as an opportunity to describe our MIP multi-scale extension for this type of simulation. We use the well-known percolation invasion method for MIP simulation [23], which uses the maximal inscribed sphere map on the pore space and the Young-Laplace inverse relationship between pore radius and pressure for capillary equilibrium. In the maximal inscribed sphere map, each pore pixel is assigned a radius value equal to the largest sphere radius that can be inscribed in that region of the pore space and includes this pixel inside the sphere. This map can be used to represent the local capillary equilibrium inter-phase between ideally wetting and non-wetting fluids, given that the contact angle of the inscribed sphere is 180°. This is a good approximation for mercury intrusion porosimetry (MIP), between the inter-phase of liquid mercury and vapour mercury. In order to minimize the surface-to-volume ratio effect given the small size of digital rock models as compared to real core samples used in the laboratory, we do not surround the whole model with mercury, but we restrict the mercury to be in contact with only one face of the rectangular prism model. For an initial low applied pressure (large applied radius), all pixels marked with radius larger or equal to the "applied radius" and connected with the inlet are marked as invaded by mercury. The applied pressure is increased and this percolation invasion process is repeated until all the pore structure is invaded. A saturation can be computed as the pore pixels invaded fraction, and recorded for each pressure. In figure 12 we show the results of this method applied to the single resolution case in our Indiana Limestone model. For the registered cases, due to the size limitations of the method, we show a 2× coarsened version of the registered model using the confocal micrite PM-type model, figure 12. For comparison, we include the experimental MIP data. We also use an experimental total porosity value of 16.5% to normalize the simulated saturations.

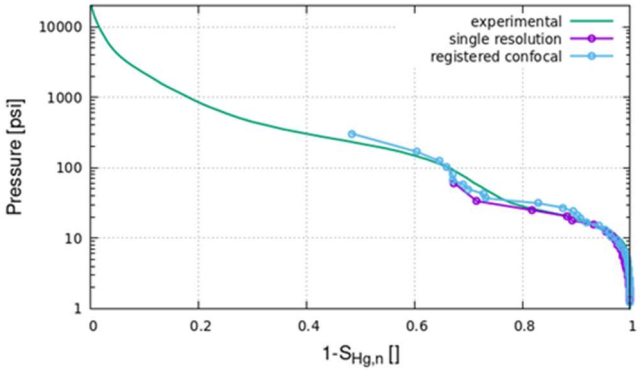

Fig. 12. Drainage results, pressure vs. normalized mercury saturation for single resolution model and registered model compared to experimental MIP.

Notice in figure 12 that the simulation results have an intrinsic maximum pressure limit associated with the minimum pixel size of the model, due to the Young-Laplace relationship. In order to extend this method to include the PM pixels, we consider the extension of the Young-Laplace relationship to radius smaller than the pixel size for a saturation S and pressure P

$$P(\phi_i, S) = \frac{2\sigma \cos\theta J(S)}{r_e(\phi_i)} \quad (3)$$

where the effective radius of a PM pixel of porosity ϕ_i, is $r_e(\phi_i) = \sqrt{k(\phi_i)/\phi_i}$, σ is the interfacial tension, θ is the contact angle, and $J(S)$ is the Leverett J-function that can be computed from the single-scale MIP simulation results on a 3D PM sample, like the micrite PM-type sample shown in figure 7. The results of this extended method that considers capillary behavior in PM pixel is shown in figure 13, where we show the MIP-PM simulation results using the confocal PM model.

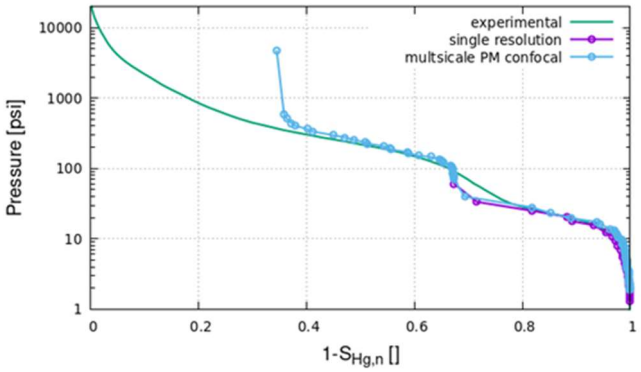

Fig. 13. Drainage results, pressure vs. normalized mercury saturation for single resolution model and multi-scale PM confocal MIP model compared to experimental MIP.

Similarly to what was done for the registered model, the saturation calculation is done using a total experimental porosity value of 16.5%, instead the total image porosity, which is 11% when one uses the micrite PM-type confocal model. The difference in total image porosity comes from a rescaling of the porosity input image, figure 6 (bottom-right), to have a mean value of 0.186 in order to be consistent with the porosity (and resolution) of the micrite confocal PM model used. In the case shown in figure 13, we were able to recover the location of the second entry pressure corresponding to the under-resolved micrite porosity, down to the limit imposed by the resolution of the PM model used, which is around 0.2 μm.

3.3 Multi-phase imbibition

This sub-section covers the application of our multi-scale multi-phase LBM method to the Indiana Limestone model. A full size single-scale multi-phase simulation was not possible due to the limited connectivity of the full size microCT model (critical radius of 1 pixel). A full size registered model is also impractical. Therefore, we decide to test first a smaller 100^3 sub-volume for methodology comparison, as shown in figure 14, microCT image, multi-scale PM model segmentation and porosity, single resolution model, and registered confocal model.

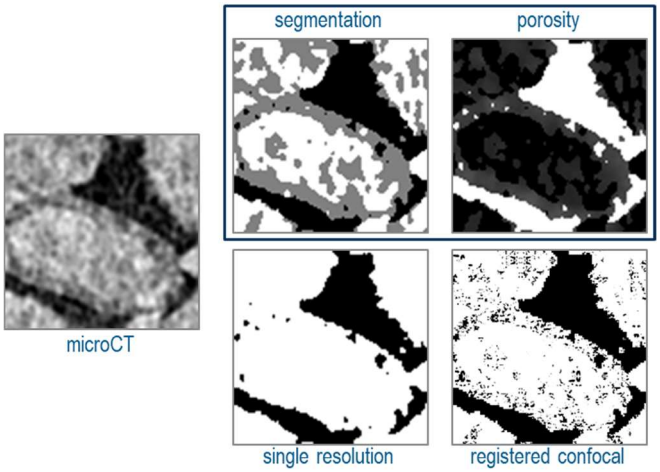

Fig. 14. Model images for the sub-volume 100^3

We considered an imbibition setup (inlet water, outlet oil) and the wettability condition was set to water wet, with a water-contacted angle 10°, oil-contacted angle 30°, and an interfacial tension water-oil 30dynes/cm. It was difficult to have a comparable initial water saturation value between models, since each one has a different effective porosity, but we tried to set it around 10%, relative to a common total porosity value used to normalize saturations to be comparable with each other. For the single resolution model and registered confocal model the 10% water saturation was set from a maximal inscribed sphere based drainage (section 3.2) and we use our single-scale LBM solver. For the multi-scale PM model the initial conditions were set with no water in the resolvable pore and a partial constant initial water saturation around 40% in the PM and our multi-scale LBM solver extension was used, with inputs: segmented and porosity images, figure 14 (top-middle and top-right), constitutive relationships for imbibition in the confocal PM model for micrite PM-type, figure 8.

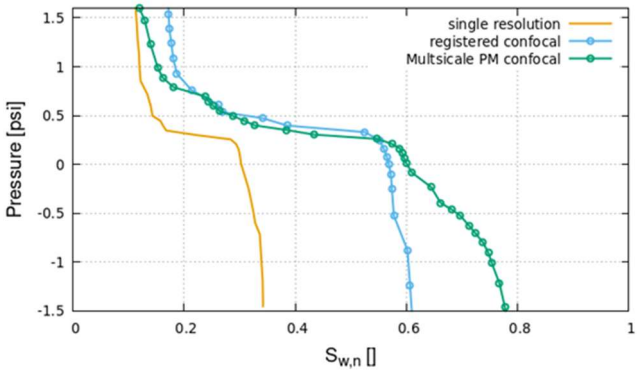

Fig. 15. Comparison of imbibition results for the sub-volume 100^3

A comparative plot with the three results is shown in figure 15, where there is a clear distinction between the single resolution model result that ignores under-resolved porosity contributions and the other two results that consider the under-resolved porosity contribution. The main difference relates to the capacity to mobilize more of the remaining oil in the pore space when the additional connectivity provided by the under-resolved porosity is considered. Notice that even though there is some variability with the registered result, there is an important consistency trend with the results obtained using the multi-scale PM-pore-solid model. The results in figure 15 provide some validation that our multi-scale multi-phase LBM extension is reasonably capturing the multi-phase behaviour as compared with some high resolution dual porosity model results, registered-confocal.

Moving up in model size, we consider next a 250^3 sub-volume scaled by 2× to a 500^3 size that shows more heterogeneity, but still keeping a minimal resolved pore connectivity, with a critical radius of 2 pixels. While not yet of REV size to compare with laboratory data, this model still gives us some additional insight on the fluids distribution at different stages of the imbibition process. This time we run only single resolution model and multi-scale model simulations. Registered models become impractical at this point. Same wettability conditions were set as in the previous case, and initial conditions were set with no water in the resolvable pore and a constant initial water saturation around 40% in the PM. In this case we use the laboratory total porosity, 16.5% to normalize all saturations.

The simulation results are shown in figure 16. First, we compare the single resolution model result (dotted yellow line) to the multi-scale result (green line), similarly to what we observed in the previous 100^3 case, the addition of the PM connectivity enables a better oil mobilization in the resolvable pores. Next, we calculate separately the saturation contributions to the multi-scale total saturation results from the resolvable pore (purple) and from PM (blue). The pore contribution starts at zero saturation, but for better visualization we move the curve to start at the same location as the PM curve. We can see that at the beginning of the simulation the PM saturation increases more than the pore

saturation, while at later stages of the simulation the order is reversed. In the bottom of figure 16 we show four stages of the fluid distribution corresponding to the green circles that also show visually the same interplay between the pore and PM water saturation evolution along the simulation.

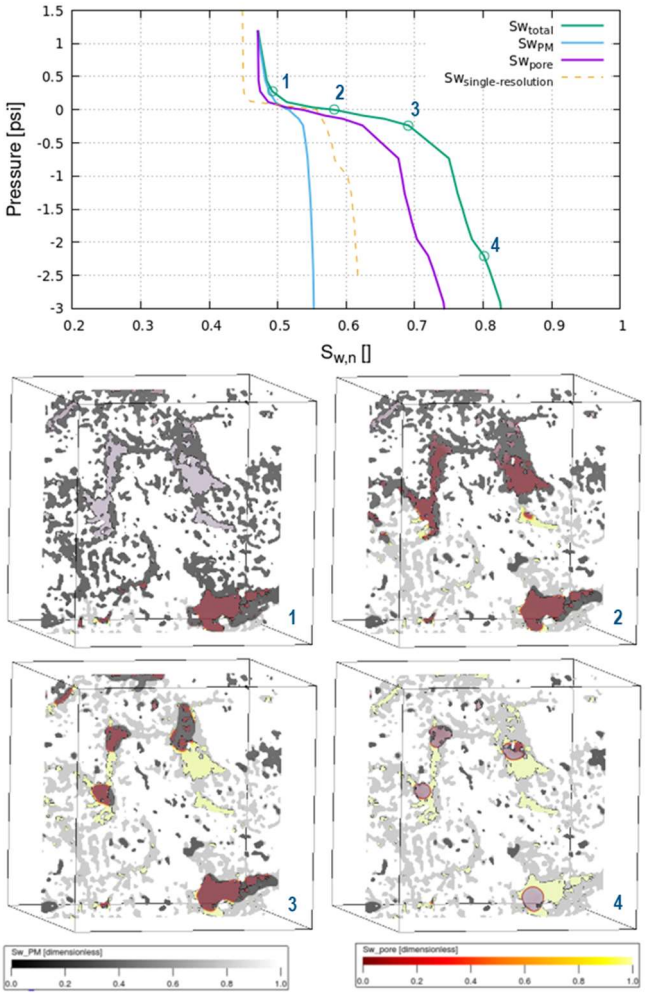

Fig. 16. Comparison of imbibition results for the 500^3 case.

Finally we run our multi-scale multi-phase simulation in the whole model 600^3 at the original resolution 3.5 μm/pixel, where the structure of only resolvable pore is barely connected by 1 pixel. We use the same initial conditions and porosity normalization as in the previous sub-volume 500^3 case. In addition to the same water-wet setup used in the two previous cases (100^3 and 500^3), we also test a mix-wet condition in which the resolvable pore is considered oil-wet, with a water-contacted angle 10°, oil-contacted angle 150°, while the PM wettability is maintained as water-wet, this is done by using the same constitutive relationships as in figure 8. In general if a different wettability condition for the PM is to be used, a new set of constitutive relationships would need to be created where the desired wettability conditions for PM are used in the simulation of the corresponding PM model.

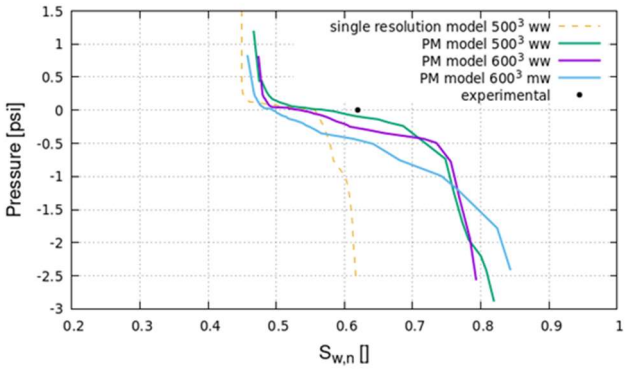

Fig. 17. Comparison of imbibition results for the 600^3 case.

Four results are shown in figure 17, a 600^3 water-wet case result (purple), two results for the sub-volume high resolution 500^3 water-wet case: single resolution model (dashed yellow) and multi-scale (green), and the 600^3 mix-wet case just described (blue). As for the water-wet cases, they are deemed to be in good agreement for the whole volume 600^3 and the 500^3 sub-volume as well as consistent with the water saturation of 62% from laboratory spontaneous imbibition measurement. Next, the mix-wet scenario behaves in the expected way relative to the water-wet case, most of the blue curve is below the purple curve, except at the end of the curve where the order is inverted. Finally, our initial observation holds: the multi-scale results show a larger mobilization of remaining oil as compared with the single-scale results.

4 Conclusions

In this paper we show a new method for multi-scale flow simulations, single-phase and multi-phase, and an application to a multi-scale carbonate rock, where under-resolved pores are believed to play an important role for oil production. We show consistency between our single-scale LBM solver and the new multi-scale LBM solver extension. In addition to an extension to the LBM solver, we also show a possible extension to include under-resolved pores to the percolation invasion method for MIP simulation that uses the maximal inscribed sphere map. It is worth noticing too that we discuss a complete workflow where a systematic identification and characterization of PM-types play a central role. Additionally, this framework allows for internal variation of porosity within the same PM-type. We believe this complete workflow represent a significant advancement in the application of digital rock methods to a difficult class of multi-scale rocks, such as carbonates. By including the simulation of flow in under resolved pores, the LBM extension solver is not limited to a minimal pixel size anymore. Given the relaxation of the resolved percolating pore space, which extend now to the join pore + PM space, other possible applications of this workflow could include plug-size sample simulation and whole core medical CT based simulation when heterogeneity is not captured properly by plug-size samples. A critical requirement could be, being able to identify PM-type classes that can be represented well by few samples at the right scale. A future workflow for core-plug and whole-core would definitely require several scales for which this workflow can be used progressively to connect pairs of adjacent scales. Multiple scales of images and other

experimental data would be necessary for testing and validation of this workflow at core-plug scale and above. The current multi-scale workflow is more suitable for isotropic uniform cases, when the under-resolved pores are much smaller than the pixel-size. Cases where the under resolved pores are close to the pixel-size would need local directionality. This limitation can be important to capture properly for instance under-resolved pore throats. We are working on an improvement that uses the image itself to compute local directionality and rotate the PM-type permeability tensor accordingly. This extension to the workflow will be the subject of a follow up publication.

References

1. G.R. Jerauld, J.T. Fredrich, N.M. Lane, Q. Sheng, B. Crouse, D.M. Freed, A. Fager, R. Xu, Abu Dhabi Int. Pet. Exhib. Conf., Society of Petroleum Engineers SPE-188688-MS (2017)
2. D.M. Freed, International Journal of Modern Physics C **09**, 1491 (1998)
3. N.S. Martys, J.G. Hagedorn, Materials and Structures **35**, 650 (2002)
4. I. Ginzburg, G. Silva, L. Talon, Phys Rev E **91**, 023307 (2015)
5. J. Li, D. Brown, Geofluids, 1740693 (2017)
6. J. Zhu, J. Ma, Scientific Reports **8** 5826 (2018)
7. A. Demianov, O. Dinariev, N. Evseev, The Canadian journal of chemical engineering **89**, 206 (2011)
8. M. Suhrer, X. Nie, J. Toelke, Proceedings of international petroleum technology conference, 20035 (2020)
9. H. Otomo, H. Chen, R. Zhang (to be published)
10. H. Otomo, R. Salazar-Tio, H. Chen, R. Zhang, A. Fager, G. Balasubramanian, B. Crouse, H. Fan, J. Yang, US patent application filing number 17/136,259 (2020)
11. H. Otomo, H. Fan, R. Hazlett, Y. Li, I. Staroselsky, R. Zhang, H. Chen, C. R. MECANIQUE **343** 559 (2015)
12. H. Otomo, H. Fan, Y. Li, M. Dressler, I. Staroselsky, R. Zhang, H. Chen, J. Comput. Sci. **17** 334 (2016)
13. H. Otomo, B. Crouse, M. Dressler, D.M. Freed, I. Staroselsky, R. Zhang, H. Chen, Comput. & Fluids **172** 674 (2018)
14. H. Chen, R. Zhang and P. Gopalakrishnan, US Patent 9576087 (2013)
15. H. Chen, R. Zhang and P. Gopalakrishnan, Phys. Scr. **95** 034003 (2020)
16. H. Chen, C. Teixeria, K. Molving, Int J Mod Phys C **9** 1281 (1998)
17. Y. Li, R. Zhang, R. Shock, H. Chen, Eur. Phys. J. Special Topics **171** 91 (2009)
18. Y. Li, R. Shock, R. Zhang, H. Chen, J.Fluid Mech **519** 273 (2004)
19. H. Fan, R. Zhang, H. Chen, Phys. Rev. E **73** 066708 (2006)
20. B. Crouse, D. M. Freed, N. Koliha, G. Balasubramanian, R. Satti, D. Bale, S. Zuklic, The Society of Core Analysis conference SCA2016-058
21. T. Bultreys. Savonnières carbonate. Digital Rocks Portal http://www.digitalrocksportal.org/projects/72 (2016)
22. S. Strebelle, Mathematical Geology **34** 1 (2002)
23. D. Silin, T. Patzek, Physica A **371** 336 (2006)
24. A. Fager, R. Salazar-Tio, G. Balasubramanian, and B. Crouse, RMAG/DWLS FALL SYMPOSIUM. Denver (2019)
25. M. Zhang, R. Salazar-Tio, A. Fager, B. Crouse, Unconventional Resources Technology Conference URTeC (2020)
26. S. K. Masalmeh, X. Jing, S. Roth, C. Wang, H. Dong, M. Blunt, Society of Petroleum engineers SPE-177572-MS (2015)
27. L. C. Ruspini, G. Lindkvist, S. Bakke, L. Alberts, A. M. Carnerup, and P. E. Øren, Society of Petroleum Engineers SPE-180268-MS (2016)
28. R. L. Folk, American Association of Petroleum Geologist Memoir **1** 62 (1962)
29. M. H. Rahman, B. J. Pierson, W. I. Yusoff, International Petroleum Technology Conference, IPTC 14583 (2011)
30. A. Ghous, T. J. Senden, R. M. Sok, A. P. Sheppard, V. W. Pinczewski, M. A. Knackstedt, Society of Petrophysicists and Well Log Analysts Symposium, Abu Dhabi, SPWLA-MERS-2007-E (2007)
31. M. A. Boone, T. De Kock, T. Bultreys, G. De Schutter, P. Vontobel, L. Van Hoorebeke, V. Cnudde, Materials Characterization, **97**, 150 (2014)
32. Q. Lin, B. Bijeljic, H. Rieke, M. J. Blunt, Water Resources Research **53**, 7457 (2017)